Identifying individual subgrains in evolving deformation structures by high angular resolution X-ray diffraction

Wejdemann, Christian; Lienert, U.; Nielsen, Hans Bruun; Pantleon, Wolfgang

Published in:
Risoe International Symposium on Materials Science. Proceedings

Publication date:
2010

Document Version
Publisher's PDF, also known as Version of record

Proceedings of the 31st
Risø International Symposium on Materials Science:
Challenges in materials science and possibilities
in 3D and 4D characterization techniques
Editors: N. Hansen, D. Juul Jensen,
S.F. Nielsen, H.F. Poulsen and B. Ralph
Risø National Laboratory for Sustainable Energy,
Technical University of Denmark, 2010

IDENTIFYING INDIVIDUAL SUBGRAINS IN EVOLVING DEFORMATION STRUCTURES BY HIGH ANGULAR RESOLUTION X-RAY DIFFRACTION

C. Wejdemann*, U. Lienert**, H. B. Nielsen*** and W. Pantleon*

* Center for Fundamental Research: Metal Structures in Four Dimensions, Materials Research Division, Risø National Laboratory for Sustainable Energy, Technical University of Denmark, Frederiksborgvej 399, 4000 Roskilde, Denmark
** Advanced Photon Source, Argonne National Laboratory, 9700 South Cass Avenue, Argonne, IL 60439, USA
*** Department of Informatics and Mathematical Modelling, Technical University of Denmark, Richard Petersens Plads, Building 321, 2800 Kgs. Lyngby, Denmark

ABSTRACT

With high angular resolution X-ray diffraction, reciprocal space maps of selected X-ray reflections from individual grains in the bulk of polycrystalline samples are obtained in situ during tensile deformation. Two different contributions are distinguished in the intensity distributions: sharp peaks of high intensity caused by diffraction from individual subgrains superimposed on a broad smoothly varying intensity distribution caused by diffraction from dislocation walls. A partitioning method using an asymmetric measure of misfit is presented for automated separation of the contributions. The peak contribution is analyzed to give detailed information about the properties of individual subgrains and their evolution with tensile deformation. Additionally, a procedure used for determining the distance of a grain from the surface of the sample along the direction of the X-ray beam is outlined.

1. INTRODUCTION

Plastic deformation of metals causes formation of defects and their arrangement in ordered structures. Deformation-induced microstructures consist of dislocation-rich walls (dislocation boundaries) separating dislocation-depleted regions of (slightly) varying orientations. Such nearly defect-free subgrains are investigated by high-angular resolution X-ray diffraction using high-energy synchrotron radiation. Reciprocal space maps of X-ray reflections from individual grains acquired with sufficiently high angular resolution reveal a number of sharp, high-intensity peaks on top of a spread-out, smoothly varying intensity distribu-

tion (Jakobsen, Poulsen, Lienert, Almer, Shastri, Sørensen, Gundlach and Pantleon 2006). The latter (called the cloud contribution) is caused by diffraction from disordered dislocation walls, whereas each individual sharp peak is caused by diffraction from a nearly perfect subgrain. By analyzing the high-intensity peaks and their behavior during deformation, properties of individual subgrains can be investigated and their evolution followed in situ. This paper describes the experimental technique used to obtain reciprocal space maps with high angular resolution and the partitioning method used to obtain information about individual subgrains. The application of the method to in situ tensile deformation is illustrated for subgrains from selected grains in the bulk of a polycrystalline copper specimen pre-deformed in tension.

2. EXPERIMENTAL TECHNIQUE

This section describes the experimental technique in general and its application to a specific experiment on a polycrystalline copper sample from which four grains were investigated at eight different strain levels. A method used to determine the distance from a grain to the sample surface along the direction of the X-ray beam is included.

2.1 Sample preparation. The sample used in the experiment is spark cut from a sheet of 99.99% pure, weakly textured, recrystallized copper with a mean grain size of approximately 20 μm. In order to introduce a dislocation structure in the material, the sheet with dimensions of 300 mm x 50 mm x 0.31 mm is pre-deformed in tension to a plastic strain of 5% with a strain rate of $1.4 \cdot 10^{-4}$ s^{-1}. The sample is cut in a dog-bone shape with a gauge length of 8 mm, a gauge width of 3 mm, and a thickness of 0.31 mm. It is oriented with the tensile axis parallel to the pre-deformation tensile axis.

2.2 Setup. A special setup for obtaining high-resolution three-dimensional reciprocal space maps from individual bulk grains while deforming the sample in tension has been developed at the Advanced Photon Source (beamline 1-ID-XOR) (Jakobsen, Poulsen, Lienert, Almer, Shastri, Sørensen, Gundlach and Pantleon 2006, Jakobsen, Poulsen, Lienert and Pantleon 2007, Jakobsen 2007). The setup includes an optical system combining a bent double-Laue pre-monochromator, collimating compound refractive lenses, a four-reflection flat-crystal high-resolution monochromator ($\Delta E/E = 7 \cdot 10^{-5}$), and a set of saw tooth lenses for vertical focusing (Shastri, Fezzaa, Mashayekhi, Lee, Fernandez and Lee 2002, Shastri 2004, Shastri, Almer, Ribbing and Cederström 2007). This increases the flux at the sample and makes it possible to acquire the same integrated intensity with a reduced acquisition time compared to a situation without focusing. The X-rays have an energy of 52 keV, giving a penetration depth in copper of approximately 500 μm, making it possible to obtain diffraction patterns from bulk grains.

The size of the beam at the sample is determined by a set of slits with a horizontal and vertical opening of 30 μm placed approximately 19 m from the optical system and 20 cm in front of the sample. The horizontal beam divergence is approximately 11 μrad, and the vertical beam divergence is approximately 17 μrad. Due to the vertical focusing, the beam height at the sample has a full width at half maximum of approximately 25 μm. The narrow beam ensures that only a small volume of the sample is illuminated so overlap with reflections from other grains is minimized. The vertical position of the beam is continuously monitored by a split ion chamber placed in front of the slits (on the same optical table) and is kept constant via a feedback loop connected to the output of the high-resolution monochromator. Between the split ion champer and the slits a fast shutter is placed to accurately control the timing of illumination.

The sample, with a resistive strain gauge glued onto the gauge area, is mounted in a custom made, screw-driven load frame, which is placed on three perpendicular translation stages and fixed to a three-axis Euler cradle. The Euler cradle is mounted on the same optical table as the slits and the split ion chamber, and its center of rotation is centered with respect to the beam. A beam stop with a Si pin diode is placed behind the sample to measure the transmitted intensity.

Two detectors are included in the setup. A large area detector (GE Revolution 41RT, 2048×2048 pixels, pixel size 200 μm), is mounted approximately 680 mm behind the sample and is used for finding suitable grains. A smaller detector (Mar CCD165, 2048×2048 pixels, pixel size 79 μm, point spread function FWHM 100 μm), is mounted above the beam approximately 3.6 m behind the sample at the height of a 400 reflection from copper and is used for obtaining high resolution reciprocal space maps. The large distance from the sample to the detector in combination with the low energy spread and the low divergence of the beam results in a high angular resolution given below. The near detector is mounted on a horizontal translation stage so it can be moved out of the X-ray path when the far detector is used.

A sketch of part of the setup is included in figure 1. The sketch includes the sample and the far detector and it shows the three coordinate axes fixed with respect to the lab: the x^L-axis is horizontal and positive to the left when looking along the beam. The y^L-axis is vertical and positive upwards. The z^L-axis is parallel to the beam and positive in the direction of the beam. The sketch also shows the three rotation axes (ω,χ,ϕ) of the Euler cradle: the outer rotation is around the ω-axis and the inner rotation is around the ϕ-axis. The ω-axis is always parallel to the x^L-axis, but the orientation of the χ- and ϕ-axes change when the sample is rotated. The center of rotation of the Euler cradle coincides with the origin of the lab coordinate system. To describe the position of grains in the sample a second coordinate system is used, which is fixed with respect to the sample and coincides with the lab system when ω, χ and ϕ are all zero. The axes of the sample system are denoted x^S, y^S and z^S. The y^S-axis is parallel to the tensile deformation axis. The detector coordinates d_x and d_y are also indicated in the sketch along with the angular coordinates 2θ and η describing the direction to a pixel from the origin of the lab system.

The high resolution reciprocal space maps are obtained in the following way: Two-dimensional images like the one shown in figure 1 are acquired on the far detector while rocking the sample (rotating it with constant angular velocity) in steps of 0.015° around the ω-axis. By stacking several images a three-dimensional reciprocal space map is built up, where two dimensions are given by the horizontal (d_x-direction) and vertical (d_y-direction) directions on the detector, and the third dimension arises from subsequent rocking intervals (ω-direction). Each point in the reciprocal space map represents the diffracted intensity integrated over a voxel in reciprocal space. The results presented in this paper are all from 400 reflections.

The resolution in 2θ is determined by the beam energy spread, the vertical beam divergence, and the width of the detector point spread function. When these contributions are added (linearly) it gives an upper limit of 0.0036°. In reciprocal space this corresponds to a resolution of $1.7 \cdot 10^{-3}$ Å^{-1} along a direction which is close to the radial direction (along the scattering vector). The resolution in η is determined by the horizontal beam divergence and the width of the detector point spread function. When these contributions are added (linearly) it gives an upper limit of 0.0086°. In reciprocal space this corresponds to a resolution of $1.0 \cdot 10^{-3}$ Å^{-1} along a direction in the azimuthal plane (the plane perpendicular to the scattering vector) normal to the plane containing the incoming and the outgoing beam (the scattering plane). The resolution in ω is determined by the rocking angle interval and

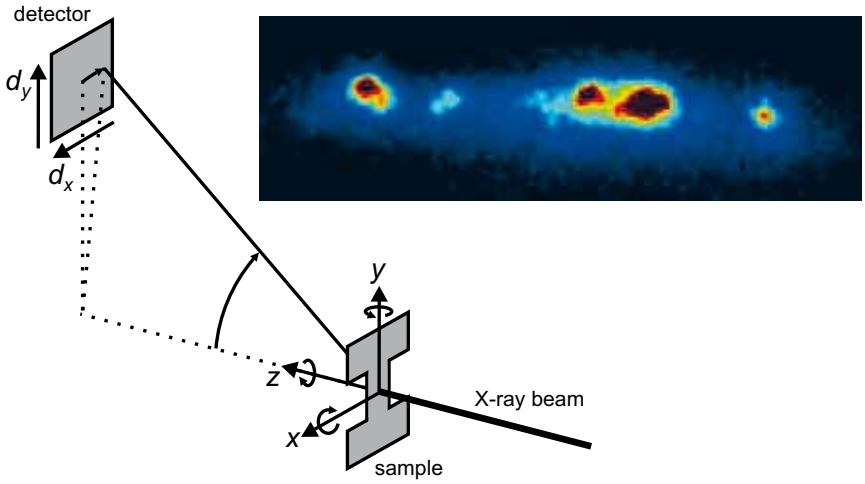

Fig. 1: Sketch of part of the setup showing the various coordinates and the diffraction geometry when the far detector is used. The lab coordinate system and the sample coordinate system coincide in the figure and are indicated by the x-, y-, and z-axes. In this case these axes are parallel to the rotation axes of the Euler cradle. The figure includes part of a two-dimensional detector image from the far detector of a 400 reflection from an individual bulk Cu grain.

is 0.015°. In reciprocal space this corresponds to a resolution of approximately $1.8 \cdot 10^{-3}$ Å^{-1} along a direction in the azimuthal plane (perpendicular to the scattering vector and in the scattering plane). The resolution in ω can be improved by using a smaller rocking angle interval at the cost of increasing the time required to acquire each reciprocal space map.

2.3 Experimental procedure. The sample is mounted in the load frame, and a small load corresponding to a strain of approximately 0.03% is applied for stabilization purposes. The sample is oriented along the axes of the sample coordinate system, centered on the center of rotation of the Euler cradle, and rotated around the ω-axis to $\omega = 7.58°$ in order to bring the in situ tensile axis (which is parallel to the y^S-axis) parallel to the scattering vector corresponding to an ideal 400 reflection from copper ($2\theta = 15.16°$) in a vertical scattering plane ($\eta = 0°$).

Four grains with their 400 direction almost parallel to (within 10°) the ideal scattering vector defined above are then selected using the near detector. Grains are excluded if the 400 reflection is not well separated from reflections from other grains, if the orientation spread is very small (indicating no interesting structure) or very large (to avoid reciprocal space maps that require many images), or if the grain is too large to be completely illuminated by the beam. The grain size is estimated by scanning the grain through the beam while measuring the intensity of the 400 reflection as a function of position. Some grains are excluded because the scan through the beam shows a profile with two distinct intensity maxima indicating the presence of a twin lamellae in the grain.

For each of the selected grains the chosen reflection is rotated to the far detector, and a reciprocal space map is obtained as described above. After this, the sample is deformed in unidirectional tension with a strain rate of approximately 10^{-4} s^{-1}. At seven different additional strain levels (up to 1%) the deformation is paused while additional reciprocal

space maps of the same 400 reflections are obtained. During acquisition the load relaxes slightly, but it has recently been shown that this does not significantly alter the subgrain structure (Jakobsen, Poulsen, Lienert, Bernier, Gundlach and Pantleon 2009). Before each map is obtained, the grain position is determined by scanning the grain through the beam, and the grain is centered in the beam in order to ensure full illumination.

2.4 Determining the distance from a grain to the surface along the X-ray beam. The thickness of the samples is approximately 15 times the average grain size. With the transmission geometry it is possible to study grains whose distance to the surface is many grain diameters. To determine the position of a grain with respect to the sample surface, a simple geometric method is used. In order to describe it, the transformation from the sample coordinates (x^S, y^S, z^S) to the lab coordinates (x^L, y^L, z^L) of a grain is introduced. It is given by $(x^L, y^L, z^L)^T = R^{L\leftarrow S}(\omega, \chi, \phi) \cdot (x^S, y^S, z^S)^T$, where

$$R^{L\leftarrow S} = \begin{pmatrix} \cos(\phi)\cos(\chi) & -\sin(\chi) & \sin(\phi)\cos(\chi) \\ \cos(\phi)\sin(\chi)\cos(\omega) - \sin(\phi)\sin(\omega) & \cos(\chi)\cos(\omega) & \sin(\phi)\sin(\chi)\cos(\omega) + \cos(\phi)\sin(\omega) \\ -\cos(\phi)\sin(\chi)\sin(\omega) - \sin(\phi)\cos(\omega) & -\cos(\chi)\sin(\omega) & -\sin(\phi)\sin(\chi)\sin(\omega) + \cos(\phi)\cos(\omega) \end{pmatrix} \quad (1)$$

is the transformation matrix, and the superscript T denotes transposition.

First the grain with sample coordinates (x^S, y^S, z^S) is centered in the beam by measuring the intensity of a reflection as a function of the grain position. Because the center of rotation of the Euler cradle is centered with respect to the beam, this means that x^L and y^L for the grain are both zero:

$$(0, 0, z_1^L)^T = R^{L\leftarrow S}(\omega_1, \chi_1, \phi_1) \cdot (x^S, y^S, z^S)^T, \quad (2)$$

where the subscript 1 indicates the parameter values corresponding to the first position and orientation.

The orientation of the sample is then changed, and this will in general move the grain out of the beam. If the grain satisfies the diffraction condition in the new orientation, the grain can be brought back to the center of the beam by translating the sample along the x^S- and y^S-axes while measuring the diffracted intensity. The shifts necessary to do this are denoted by Δx^S and Δy^S. The sample coordinates of the grain after the translation are $(x^S + \Delta x^S, y^S + \Delta y^S, z^S)$, and they satisfy the equation

$$(0, 0, z_2^L)^T = R^{L\leftarrow S}(\omega_2, \chi_2, \phi_2) \cdot (x^S + \Delta x^S, y^S + \Delta y^S, z^S)^T. \quad (3)$$

Equations (2) and (3) contain the three equations:

$$x^S \cos(\phi_1)\cos(\chi_1) - y^S \sin(\chi_1) + z^S \sin(\phi_1)\cos(\chi_1) = 0 \quad (4)$$

$$x^S(\cos(\phi_1)\sin(\chi_1)\cos(\omega_1) - \sin(\phi_1)\sin(\omega_1)) + y^S \cos(\chi_1)\cos(\omega_1) + z^S(\sin(\phi_1)\sin(\chi_1)\cos(\omega_1) + \cos(\phi_1)\sin(\omega_1)) = 0 \quad (5)$$

$$(x^S + \Delta x^S)\cos(\phi_2)\cos(\chi_2) - (y^S + \Delta y^S)\sin(\chi_2) + z^S \sin(\phi_2)\cos(\chi_2) = 0. \quad (6)$$

When the rotation parameters ω_1, χ_1, ϕ_1, χ_2, and ϕ_2 are known and the shifts Δx^S and Δy^S are measured, equations (4-6) can be solved for the grain sample coordinates (x^S, y^S, z^S). z^S is the distance of the grain along the z^S-axis from the center of rotation, and knowing the position of the sample with respect to the center of rotation, the distance of the grain from the surface can be calculated.

In order to use the method, it is necessary to find a second orientation of the grain in which the used reflection satisfies the diffraction condition. If the angular coordinates of

the reflection in the first orientation are (2θ,η), the corresponding reciprocal lattice vector, G, has length $|G| = 4\pi \sin(\theta)/\lambda$ (where λ is the X-ray wavelength) and lab coordinates

$$G_1^L = \left(G_{x,1}^L, G_{y,1}^L, G_{z,1}^L\right) = \left(- |G| \cos(\theta) \sin(\eta), |G| \cos(\theta) \cos(\eta), -|G| \sin(\theta)\right). \quad (7)$$

The lab coordinates of G in the second orientation are

$$G_2^L = R^{L \leftarrow S}(\omega_2, \chi_2, \phi_2)\left(R^{L \leftarrow S}(\omega_1, \chi_1, \phi_1)\right)^{-1} G_1^L. \quad (8)$$

Because of the geometry of the setup the value of χ has no effect on the position of the grain with respect to the beam and need not be changed during the rotation. It is then straightforward, based on equation (8), to numerically calculate all the combinations ω_2 and ϕ_2 for which the reciprocal lattice vector satisfies the diffraction condition $G_{z,2}^L = G_{z,1}^L = -|G| \sin(\theta)$.

3. DATA ANALYSIS

This section describes the pre-processing of the two-dimensional images, presents an interpretation of the reciprocal space maps in terms of contributions from the dislocation-dense and dislocation-free regions of the grain respectively, and describes a newly developed method for partitioning the intensity distribution into these two contributions.

3.1 Pre-processing of the images. Before the individual images are stacked, they are subjected to three pre-processing steps. First, the mean background level around the 400 reflection is estimated for each image and subtracted from the intensity. Second, the intensity in the image is normalized with the beam intensity measured at the beam stop behind the sample during acquisition. Third, cosmic rays are identified in each image by comparing the intensity on a pixel by pixel basis with the images taken just before and after. If found, cosmic rays are removed by linear interpolation between those neighboring images.

The two-dimensional images are then stacked along the ω-direction to produce a three-dimensional reciprocal space map. Three-dimensional maps are difficult to visualize, but the intensity distributions are much narrower in the d_y-direction than in the d_x- and ω-directions and therefore a good overview can be obtained from projections onto the d_x-ω-plane. The result of this is called an azimuthal map here because the deviation from an azimuthal projection in reciprocal space is very small. The azimuthal map corresponds to a 400 pole figure for the grain and shows the distribution of the 400-direction (the mosaic spread) within the grain. Examples of azimuthal maps are shown in figures 2 and 4.

3.2 Interpretation of the reciprocal space maps. The high angular resolution achieved with the setup described above makes it possible to observe features in the reciprocal space maps which are not seen in traditional diffraction experiments. Generally, the intensity distributions can be described as being composed of two contributions: a spread-out, smoothly varying component (here called the cloud component) and a component consisting of a number of sharp high-intensity peaks (here called the peak component). The heterogeneous structure of the intensity distribution with peaks superimposed on a low-intensity spread-out cloud can be seen both in the detector image in figure 1 and the azimuthal maps in figures 2 and 4. The interpretation of these features is that the spread-out cloud is caused by diffraction from dislocation-dense regions (the dislocation walls) and each sharp peak is caused by diffraction from an almost dislocation-free region (a subgrains) (Jakobsen et al. 2006, Jakobsen et al. 2007, Jakobsen, Lienert, Almer, Poulsen, and Pantleon 2008). This interpretation has been confirmed by spatially-resolved observations (Levine, Larson, Yang,

Kassner, Tischler, Delos-Reyes, Fields, and Liu 2006, Levine, Larson, Tischler, Geantil, Kassner, Liu, and Stoudt 2008).

3.3 Partitioning the reciprocal space maps. It is desirable to partition the intensity distributions into two parts corresponding to the two contributions described above, as this will allow analysis of each part separately, specifically the properties of individual peaks corresponding to individual subgrains. Such a partitioning is a challenging task because of the widely differing shapes, sizes and background level (the cloud intensity) of the peaks. For this purpose a fitting method has been developed, that relies on approximating the cloud component with a smooth function. The method uses an asymmetric measure of misfit to generate a fit that approximates the cloud only and ignores the high-intensity peaks as sketched in the top left part of figure 2. The result is a model of the cloud contribution, which is subtracted from the total intensity distribution to give a model for the peak component.

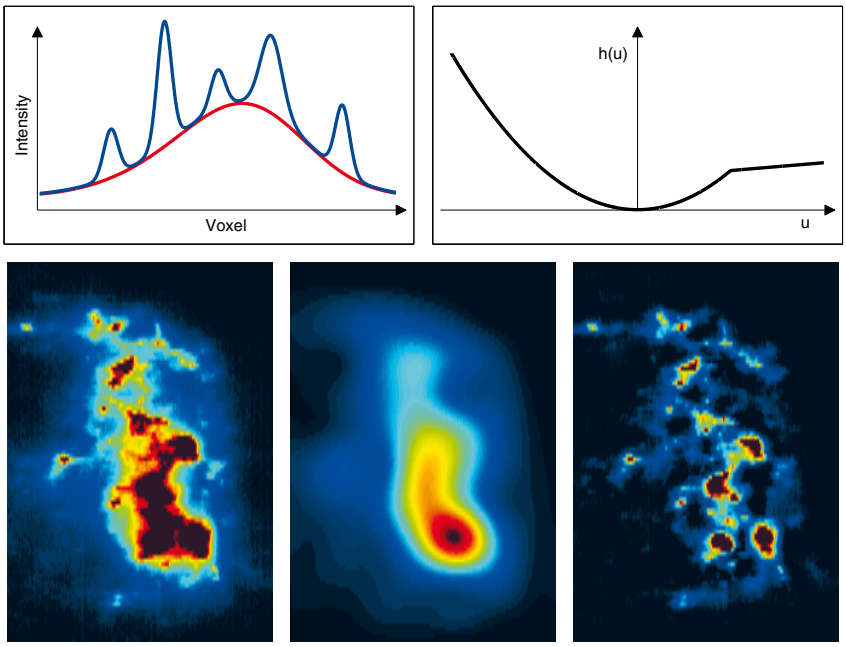

Fig. 2: Top left: Sketch of partitioning method. Top right: Sketch of the function $h(u)$. Bottom: Azimuthal maps from one grain showing the original data (left) and models of the cloud (left) and peak (right) components. The d_x-direction is horizontal and the ω-direction is vertical. The pixels are stretched to give similar reciprocal space resolutions in the two directions.

Because of the computational cost involved, the fitting is performed on individual d_x-ω-planes, and the results are stacked (along the d_y-direction) to produce a three-dimensional model of the cloud contribution. The required computing time is further cut down by reducing the data sets before the partitioning. This is done by dividing each azimuthal plane into a set of equal sized rectangles and replacing each rectangle with a single data point having the average value of the pixels in the rectangle. The rectangles are 6 voxels in the d_x-direction and 2 voxels in the ω-direction to give approximately the same reciprocal

space resolution in the two directions. The data reduction has no significant effect on the resulting cloud model.

The smooth function used in the fit for each azimuthal layer is a bicubic spline. A bicubic spline is a two-dimensional piecewise bicubic function which is continuous and has continuous first and second derivatives. The domain of the spline (the d_x-ω-plane) is divided into rectangles (not the same as above) by a regular grid defined by a set of points (called knots) in each direction (d_x and ω), and in each of the rectangles the spline is given by an expression of the form:

$$s(d_x, \omega) = \sum_{i=0}^{3} \sum_{j=0}^{3} a_{ij} d_x^i \omega^j. \tag{9}$$

The coefficients a_{ij} are different in different rectangles. At the boundary of the domain the second derivative of the spline is set to zero. The knot distances are important parameters that have a rather large effect on the resulting cloud model. The smaller the knot distance, the better the spline is able to follow variations in the intensity distribution. Based on visual inspection of one-dimensional intensity profiles through the reciprocal space maps and the corresponding cloud model, the knot distances are chosen to give the 'right' amount of flexibility in the splines. Knot distances of 30 voxels in the d_x-direction and 10 voxels in the ω-direction are used to give approximately the same reciprocal space resolution in the two directions.

To produce a good model of the cloud component the splines should follow the smoothly varying part of the intensity distribution and ignore the high-intensity peaks as in the sketch in the top left part of figure 2. This is achieved by using an asymmetric measure of misfit, h, when fitting the spline to the (reduced) data points. The function h is given by

$$h(u) = \begin{cases} u^2/2\gamma & \text{for} \quad u \leq \gamma \\ \alpha u/\gamma + \gamma/2 - \alpha & \text{for} \quad u > \gamma \end{cases}, \tag{10}$$

where $u = d - s$ is the difference between the data value and the value of the spline. The function is sketched in the top right part of figure 2. This measure of misfit is inspired by the one-sided Huber method described by Bandler, Chen, Biernacki, Gao, Madsen, and Yu (1993). The method differs from conventional least squares fitting for data points for which $d - s > \gamma$. These are assigned a much smaller measure of misfit and hence do not influence the fit very much. The parameter γ sets the scale for the smallest peaks that can be separated from the background, and the value of γ should be of the order of the noise in the data. If γ is too small, fluctuations due to noise will be treated as peaks, and if γ is too large, the smallest peaks will be treated as fluctuations in the cloud caused by noise. The exact value has only a small effect on the resulting could model. Here $\gamma = 5$ is used which is approximately twice the standard deviation of the random pixel-to-pixel variation in the background. The parameter α determines the relative influence of data points for which $d - s > \gamma$ (points in the peaks) and has a rather large effect on the resulting cloud model. Here $\alpha = 0.5$ is used. Like the knot distances, the values of γ and α are chosen based on visual inspection of the results. More details can be found in Wejdemann (2010).

Based on the function h, the model of the cloud component is the solution obtained by varying the coefficients a_{ij} for the bicubic spline to minimize the sum $\sum_k h(d_k - s_k)$ over all (reduced) data points. Here d_k is the k'th data point, and s_k is the value of the spline at the same point. To find the solution, an algorithm developed by Madsen and Nielsen (1990) is used. When the solution is found, the spline is subtracted from the original reciprocal space map (not the reduced data) to produce a model of the peak component. An example is shown in the bottom part of figure 2.

4. RESULTS AND DISCUSSION

Reciprocal space maps of a 400 reflection close to the tensile axis are acquired and analyzed for all four selected grains at eight different strain values. All four grains behave qualitatively similar and only the results from one of the selected grains are presented. For this grain the distance to the surface is found to be 120 μm by the method described in section 2.4.

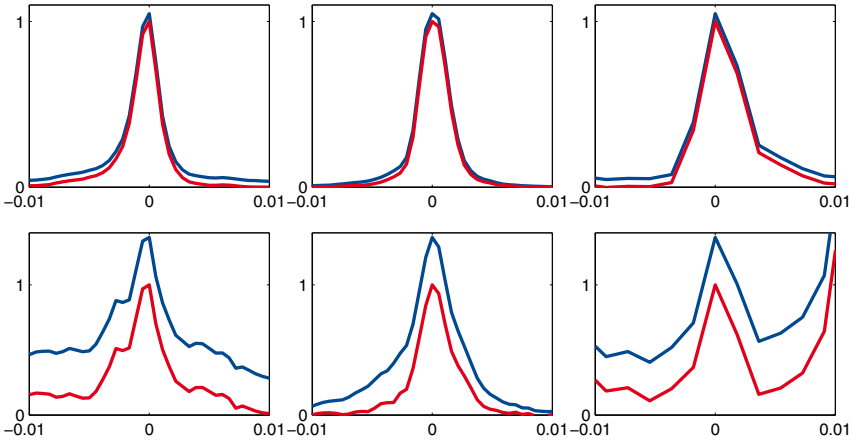

Fig. 3: One-dimensional profiles for two individual peaks before (blue) and after (red) partitioning. Shown are profiles along the d_x- (left), d_y- (center), and ω-direction (right) for a relatively strong (top) and a relatively weak (bottom) peak. The horizontal axes show distances in reciprocal space measured from the peak center in units of Å^{-1}. The vertical axes show the intensity normalized to the maximum intensity in the peak after partitioning.

High-intensity peaks can be readily identified in the reciprocal space maps and their intensity distribution can be characterized by intensity profiles along different directions in reciprocal space. One-dimensional profiles are made along the d_x-, d_y-, and ω-direction of the reciprocal space maps (through one row or column of voxels). The d_x- and ω-directions are almost in the azimuthal plane and the d_y-direction is almost along the radial direction. For two high-intensity peaks, such one-dimensional intensity profiles before and after removal of the underlying cloud contribution are shown in figure 3. The intensity profiles for both subgrains presented are rather sharp and the widths in all three directions of reciprocal space are comparable. From such intensity profiles, the average position of each high-intensity peak in reciprocal space can be determined for each deformation step. In this manner, changes in the elastic strains of individual subgrains (from the radial position of the peaks) and their re-orientation (from their azimuthal position) can be followed with increasing plastic deformation.

Azimuthal maps of only the peak component for one grain at six different strain values are shown in figure 4. Several distinct high-intensity peaks can be identified corresponding to subgrains of different orientations. These subgrains experience rather different elastic strains which is apparent from the different d_y positions in the detector image in figure and which can be quantified from the radial intensity distributions.

Some of the high-intensity peaks can be recognized in all deformation steps throughout the

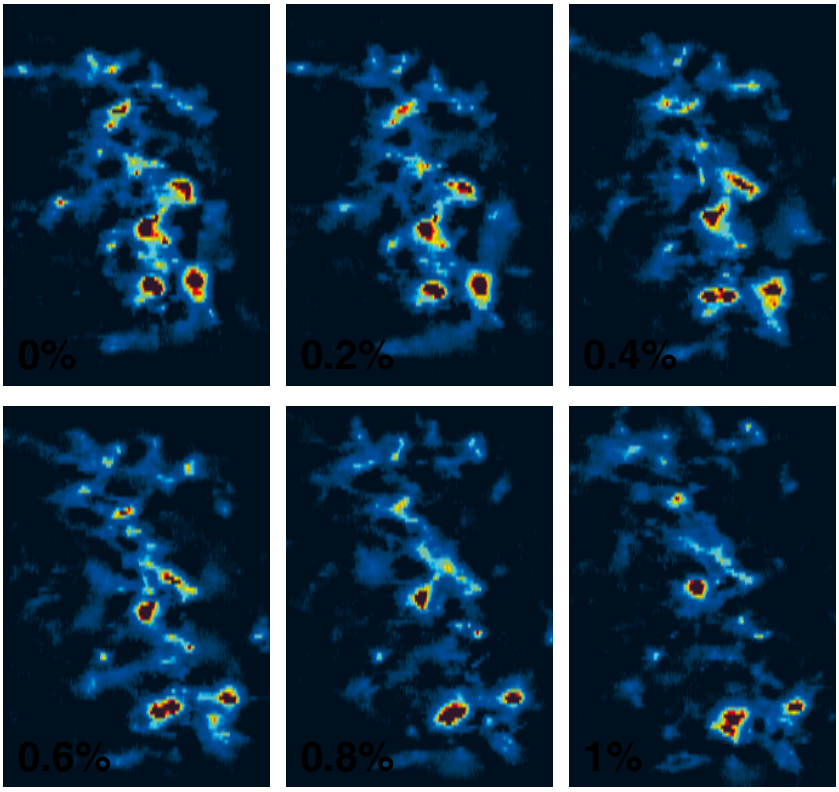

Fig. 4: Azimuthal maps of the peak component from one grain for different strain values indicated on the maps. The d_x-direction is horizontal and the ω-direction is vertical. The maps all show regions of reciprocal space of the same size. The pixels are stretched to give similar reciprocal space resolutions in the two directions.

in situ deformation. Closer inspection of the images reveals that these peaks move with respect to each other in reciprocal space. The orientation differences between the corresponding subgrains increase according to the increasing distance between their 400 poles. Concurrently, some of the other high-intensity peaks lose intensity and even disappear; the related subgrains shrink in size and even dissolve with proceeding deformation.

5. SUMMARY

With high resolution reciprocal space mapping using high energy X-rays, individual subgrains can be revealed in selected grains in the bulk of polycrystalline samples and followed during tensile deformation. It is possible to determine that a selected grain is sufficiently far from the sample surface to represent bulk behavior by a simple geometric method. A partitioning method is presented that allows the diffracted intensity from subgrains to be separated from the contribution from the dislocation walls. From the subgrain intensity distribution, individual peaks are singled out and analyzed separately to gain information about the properties of individual subgrains such as their orientation and the elastic strain along the tensile axis.

ACKNOWLEDGEMENT

The authors wish to thank L. Lorentzen, F. Adrian and P. Olesen for sample preparation and characterization. This work was supported by the Danish National Research Foundation and the Danish Natural Science Research Council. Use of the Advanced Photon Source was supported by the U.S. Department of Energy, Office of Science, Office of Basic Energy Sciences, under Contract No. DE-AC02-06CH11357.

REFERENCES

Bandler, J. W., Chen, S. H., Biernacki, R. M., Gao, L., Madsen, K., and Yu, H. (1993). Huber optimization of circuits: a robust approach. IEEE Trans. Microwave Theory Tech. 41, 2279-2287.

Jakobsen, B., Poulsen, H. F., Lienert, U., Almer, J., Shastri, S. D., Sørensen. H. O., Gundlach, C., and Pantleon, W. (2006). Formation and subdivision of deformation structures during plastic deformation. Science 312, 889-892.

Jakobsen, B., Poulsen, H. F., Lienert, U., and Pantleon, W. (2007). Direct determination of elastic strains and dislocation densities in individual subgrains in deformation structures. Acta Mater. 55, 3421-3430.

Jakobsen, B., Lienert, U., Almer, J., Poulsen, H. F., and Pantleon, W. (2008). Direct observation of strain in bulk subgrains and dislocation walls by high angular resolution three-dimensional X-ray diffraction. Mater. Sci. Eng. A 483484, 641-643.

Jakobsen, B., Poulsen, H. F., Lienert, U., Bernier, J., Gundlach, C., and Pantleon, W. (2009). Stability of dislocation structures in copper towards stress relaxation investigated by high angular resolution 3D X-ray diffraction. Phys. Status Solidi A 206, 2130.

Levine, L. E., Larson, B. C., Yang, W., Kassner, M. E., Tischler, J. Z., Delos-Reyes, M. A., Fields, R. J., and Liu, W. (2006). X-ray microbeam measurements of individual dislocation cell elastic strains in deformed single-crystal copper. Nat. Mater. 5, 619-622.

Levine, L. E., Larson, B. C., Tischler, J. Z., Geantil, P., Kassner, M. E., Liu, W, and Stoudt, M. R. (2008). Impact of dislocation cell elastic strain variations on line profiles from deformed copper. Z. Kristallogr. Suppl. 27, 55-63.

Madsen, K., and Nielsen, H. B. (1990). Finite algorithms for robust linear regression. BIT 30, 682-699.

Shastri, S. D., Fezzaa, K., Mashayekhi, A., Lee, W.-K., Fernandez, P. B., and Lee, P. L. (2002). Cryogenically cooled bent double-Laue monochromator for high-energy undulator X-rays (50-200 keV). J. Synchrotron Rad. 9, 317-322.

Shastri, S. D. (2004). Combining flat crystals, bent crystals and compound refractive lenses for high-energy X-ray optics. J. Synchrotron Rad. 11, 150-156.

Shastri, S. D., Almer, J., Ribbing, C., and Cederström, B. (2007). High-energy X-ray optics with silicon saw-tooth refractive lenses. J. Synchrotron Rad. 14, 204-211.

Wejdemann, C. (2010). Evolution of dislocation structures following a change in loading conditions studied by in situ high resolution reciprocal space mapping. PhD thesis. Risø DTU, Roskilde, Denmark. To be published.